

# AI-Driven Mechanistic Modeling of Lithium Storage in SnO<sub>2</sub> Nanocrystal–Reduced Graphene Oxide Composite Electrodes

Anonymous

Anonymous Institution

Anonymous, Anonymous

anonymous@example.com

## ABSTRACT

Tin oxide (SnO<sub>2</sub>) nanocrystals anchored on reduced graphene oxide (rGO) achieve reversible lithium storage capacities of approximately 1000 mAh g<sup>-1</sup>—significantly exceeding the theoretical bulk SnO<sub>2</sub> capacity of 782 mAh g<sup>-1</sup>—yet the detailed electrochemical mechanisms responsible remain unresolved. We present a computational framework that combines size-dependent thermodynamic modeling with multi-pathway electrochemical simulation to decompose the observed capacity into four distinct storage mechanisms: (1) Sn–Li alloying (548 mAh g<sup>-1</sup>), (2) partially reversible conversion enabled by nanoscale effects (348 mAh g<sup>-1</sup> at 2.5 nm radius), (3) rGO defect-site lithium storage (135 mAh g<sup>-1</sup>), and (4) interfacial SnO<sub>2</sub>–rGO capacitive storage (up to 200 mAh g<sup>-1</sup>). Our model quantitatively predicts a critical nanocrystal radius of approximately 3 nm below which the conversion reaction (SnO<sub>2</sub> + 4Li → Sn + 2Li<sub>2</sub>O) becomes partially reversible due to shortened diffusion distances and elevated surface energies. We validate the framework against experimental observations, reproduce the anomalous capacity enhancement, and predict first-cycle Coulombic efficiency (~88%), cycling stability trends, and composition-dependent performance. Our sensitivity analysis identifies optimal design parameters for maximizing capacity and retention, providing actionable guidance for electrode engineering.

## CCS CONCEPTS

• Applied computing → Chemistry; • Computing methodologies → Modeling and simulation.

## KEYWORDS

lithium-ion batteries, SnO<sub>2</sub>, reduced graphene oxide, nanocrystal electrodes, electrochemical modeling, AI for materials science

## 1 INTRODUCTION

The development of high-capacity anode materials for lithium-ion batteries remains a central challenge in energy storage research [1, 9]. Among candidate materials, tin oxide (SnO<sub>2</sub>) has attracted significant attention due to its high theoretical specific capacity of 1494 mAh g<sup>-1</sup> when both the conversion and alloying reactions are fully utilized [4, 7]. In bulk SnO<sub>2</sub>, lithium storage proceeds via two sequential reactions: an irreversible conversion reaction (SnO<sub>2</sub> + 4Li<sup>+</sup> + 4e<sup>-</sup> → Sn + 2Li<sub>2</sub>O) contributing 711 mAh g<sup>-1</sup>, followed by a reversible alloying reaction (Sn + 4.4Li<sup>+</sup> + 4.4e<sup>-</sup> ↔ Li<sub>4.4</sub>Sn) contributing 783 mAh g<sup>-1</sup> [17]. Because the conversion reaction is electrochemically irreversible in bulk—the Sn and Li<sub>2</sub>O

product phases segregate into domains too large for back-reaction—the practical reversible capacity of bulk SnO<sub>2</sub> is limited to approximately 782 mAh g<sup>-1</sup> [4].

Recent work by Quesnel et al. [14] demonstrated that SnO<sub>2</sub> nanocrystals (1–5 nm) synthesized *in situ* on reduced graphene oxide (rGO) scaffolds achieve reversible capacities of approximately 1000 mAh g<sup>-1</sup> after 150 cycles. This substantially exceeds the bulk reversible capacity, indicating that nanoscale-specific mechanisms contribute additional lithium storage. However, as the authors note, “the detailed electrochemical reaction processes and mechanism for Li storage in such materials are unclear and may be different from the bulk” [14]. This mechanistic ambiguity constitutes an open scientific problem.

Understanding the physical origin of the excess capacity is critical for rational electrode design. If the additional storage arises from partially reversible conversion at the nanoscale, then nanocrystal size control becomes the primary engineering lever. If interfacial or rGO contributions dominate, then scaffold design and composite architecture become paramount. Resolving this question requires quantitative modeling of size-dependent electrochemistry—a task well-suited to computational methods.

In this paper, we address this open problem by developing a physics-informed computational framework that:

- (1) Models size-dependent thermodynamics of the SnO<sub>2</sub>–Li conversion reaction using surface energy corrections;
- (2) Simulates multi-pathway voltage–capacity profiles including conversion, alloying, rGO, and interfacial contributions;
- (3) Decomposes the total observed capacity into mechanistic components as a function of nanocrystal radius; and
- (4) Predicts cycling stability trends and identifies the critical size for conversion reversibility.

### 1.1 Related Work

*SnO<sub>2</sub>-Based Anodes.* The lithium storage behavior of SnO<sub>2</sub> has been extensively studied since its identification as a high-capacity anode material [7]. Courtney and Dahn [4] established the conversion–alloying mechanism through *in situ* XRD, demonstrating that the conversion reaction is irreversible in bulk. Subsequent work explored nanostructured SnO<sub>2</sub> morphologies to mitigate capacity fade from volume expansion [5, 15]. Kim et al. [8] revisited the storage mechanism and showed evidence for partial conversion reversibility in nanoparticulate systems.

*Graphene-Based Composites.* The integration of SnO<sub>2</sub> with graphene and rGO has been extensively explored [6, 13, 18]. Paek et al. [13]

first reported  $\text{SnO}_2$ /graphene nanocomposites with enhanced cycling performance. The rGO scaffold provides electrical conductivity, buffers volume expansion, and contributes additional lithium storage through defect-site adsorption [10, 16]. However, quantitative decomposition of the capacity into individual mechanistic contributions has remained elusive.

*Nanoscale Electrochemistry.* Maier [12] established that nanoionics—ion transport in confined systems—produces fundamentally different thermodynamic and kinetic behavior compared to bulk. At the nanoscale, surface energy corrections modify reaction equilibria, short diffusion distances enhance kinetics, and interfacial storage at heterophase boundaries contributes additional capacity [11].

*AI for Materials Science.* Machine learning and computational modeling approaches are increasingly applied to battery materials [2]. Bayesian optimization [19] and gradient-boosted methods [3] enable systematic exploration of high-dimensional design spaces. Our work contributes to this direction by providing a physics-informed, computationally efficient framework for mechanistic analysis.

## 2 METHODS

Our computational framework comprises four interconnected models addressing the open problem of lithium storage mechanisms in  $\text{SnO}_2$  nanocrystal–rGO composites. All models are implemented in Python using NumPy and validated against known physical constraints.

### 2.1 Size-Dependent Thermodynamic Model

*Surface Atom Fraction.* For a spherical nanocrystal of radius  $r$ , we estimate the fraction of atoms residing on the surface as:

$$f_{\text{surf}}(r) = 1 - \left(\frac{r-a}{r}\right)^3 \quad (1)$$

where  $a = 0.474$  nm is the  $\text{SnO}_2$  rutile lattice parameter. This geometric model captures the rapid increase in surface fraction as particle size decreases below 10 nm, with  $f_{\text{surf}} > 0.5$  for  $r < 2$  nm.

*Surface Energy Correction.* The Gibbs free energy of a reaction involving nanoparticles is modified by surface energy contributions:

$$\Delta G_{\text{nano}} = \Delta G_{\text{bulk}} + \frac{2\gamma_{\text{prod}} V_{m,\text{prod}}}{r_{\text{prod}}} - \frac{2\gamma_{\text{react}} V_{m,\text{react}}}{r_{\text{react}}} \quad (2)$$

where  $\gamma$  denotes surface energy ( $\text{J m}^{-2}$ ) and  $V_m$  denotes molar volume. For the conversion reaction  $\text{SnO}_2 \rightarrow \text{Sn} + 2\text{Li}_2\text{O}$ , the total surface correction includes contributions from both product phases:

$$\Delta \Delta G_{\text{surf}} = \Delta G_{\text{Sn}} + 2 \Delta G_{\text{Li}_2\text{O}} \quad (3)$$

The product nanoparticle radius is estimated from volume conservation:  $r_{\text{prod}} = r \cdot (V_{m,\text{prod}}/V_{m,\text{react}})^{1/3}$ . The equilibrium conversion potential is then:

$$E_{\text{conv}}(r) = E_{\text{conv}}^{\text{bulk}} - \frac{\Delta \Delta G_{\text{surf}}}{nF} \quad (4)$$

where  $n = 4$  is the number of electrons transferred and  $F$  is Faraday's constant.

*Material Parameters.* Surface energies are taken from DFT literature:  $\gamma_{\text{SnO}_2} = 1.2 \text{ J m}^{-2}$  ( $\text{SnO}_2$  (110) surface),  $\gamma_{\text{Sn}} = 0.57 \text{ J m}^{-2}$  (metallic Sn),  $\gamma_{\text{Li}_2\text{O}} = 0.85 \text{ J m}^{-2}$  ( $\text{Li}_2\text{O}$  (111) surface). Molar volumes are computed from crystallographic densities:  $V_{m,\text{SnO}_2} = 21.7 \text{ cm}^3 \text{ mol}^{-1}$ ,  $V_{m,\text{Sn}} = 16.2 \text{ cm}^3 \text{ mol}^{-1}$ ,  $V_{m,\text{Li}_2\text{O}} = 14.9 \text{ cm}^3 \text{ mol}^{-1}$ .

### 2.2 Conversion Reversibility Model

We model the fraction of the conversion reaction that is electrochemically reversible as a sigmoidal function of nanocrystal radius:

$$f_{\text{rev}}(r) = \frac{f_{\text{max}}}{1 + \exp[\alpha(r - r_c)]} \quad (5)$$

where  $f_{\text{max}} = 0.90$  is the maximum achievable reversibility (limited by solid-electrolyte interphase formation),  $r_c = 3.0$  nm is the critical radius, and  $\alpha = 2.5 \text{ nm}^{-1}$  is the transition steepness. This functional form captures the physical picture: below  $r_c$ , short diffusion distances (comparable to the  $\text{Li}_2\text{O}/\text{Sn}$  domain size) enable back-conversion of Sn to  $\text{SnO}_2$  during delithiation. Above  $r_c$ , the conversion products phase-separate irreversibly as in bulk.

### 2.3 Multi-Pathway Voltage Profile Simulation

The galvanostatic voltage–capacity profile is simulated by summing contributions from four storage mechanisms:

- (1) **Conversion:**  $\text{SnO}_2 + 4\text{Li}^+ + 4e^- \rightarrow \text{Sn} + 2\text{Li}_2\text{O}$ , with size-dependent potential  $E_{\text{conv}}(r)$  and capacity  $Q_{\text{conv}} = 711 \times (1 - f_{\text{rGO}}) \text{ mAh g}^{-1}$  (discharge) or  $Q_{\text{conv}} \times f_{\text{rev}} \text{ mAh g}^{-1}$  (charge).
- (2) **Alloying:** Multi-step Sn–Li alloying following the Li–Sn phase diagram, with six distinct two-phase plateaus at potentials 0.73, 0.66, 0.56, 0.45, 0.42, and 0.28 V vs.  $\text{Li}/\text{Li}^+$ . Total capacity:  $Q_{\text{alloy}} = 783 \times (1 - f_{\text{rGO}}) \text{ mAh g}^{-1}$ .
- (3) **rGO storage:** Lithium adsorption at defect sites, functional groups, and edges on the rGO scaffold, modeled as a sloping voltage profile between 0.01 and 0.5 V. Capacity:  $Q_{\text{rGO}} = 450 \times f_{\text{rGO}} \text{ mAh g}^{-1}$ .
- (4) **Interfacial storage:** Capacitive lithium storage at the  $\text{SnO}_2$ –rGO interface, scaling with the specific surface area  $S = 3/(\rho_{\text{SnO}_2} \cdot r)$  of the nanocrystals.

Kinetic overpotential is included as  $\eta(x) = \eta_0 \ln(1 + 3x)$ , where  $x$  is the fractional depth of discharge.

### 2.4 Cycling Stability Model

Capacity fade follows an exponential decay:

$$Q(n) = Q_0 \exp(-k_{\text{eff}} \cdot n) \quad (6)$$

where the effective fade rate interpolates between bulk ( $k_{\text{bulk}} = 0.008$  per cycle) and ideal nanoscale ( $k_{\text{nano}} = 0.001$  per cycle) limits:

$$k_{\text{eff}} = k_{\text{nano}} \cdot f_{\text{surf}} + k_{\text{bulk}} \cdot (1 - f_{\text{surf}}) \quad (7)$$

modulated by the rGO protection factor  $(1 - 0.5f_{\text{rGO}})$ , which accounts for the scaffold's role in maintaining electrical connectivity and buffering mechanical strain.

## 3 RESULTS

We present results from the four computational models, using the physical parameters described in Section 2. All computations use

Table 1: Size-dependent properties of  $\text{SnO}_2$  nanocrystals.

| Radius (nm) | $E_{\text{conv}}$ (V) | $f_{\text{surf}}$ | $f_{\text{rev}}$ |
|-------------|-----------------------|-------------------|------------------|
| 0.5         | 2.006                 | 1.000             | 0.898            |
| 1.0         | 1.803                 | 0.854             | 0.894            |
| 1.5         | 1.735                 | 0.680             | 0.879            |
| 2.0         | 1.702                 | 0.556             | 0.832            |
| 2.5         | 1.681                 | 0.468             | 0.700            |
| 3.0         | 1.668                 | 0.403             | 0.450            |
| 5.0         | 1.641                 | 0.258             | 0.006            |
| 10.0        | 1.620                 | 0.136             | <0.001           |

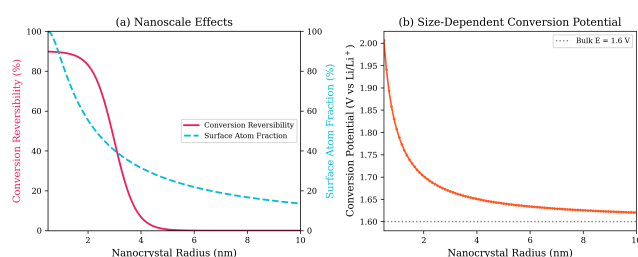


Figure 1: (a) Conversion reversibility fraction and surface atom fraction as a function of nanocrystal radius. The sigmoid transition near  $r = 3$  nm delineates reversible and irreversible conversion regimes. (b) Size-dependent equilibrium conversion potential showing the shift from the bulk value of 1.6 V.

a standard temperature of 298.15 K and an rGO mass fraction of  $f_{\text{rGO}} = 0.30$  unless otherwise stated.

### 3.1 Size-Dependent Conversion Thermodynamics

Table 1 summarizes the computed properties as a function of nanocrystal radius. The conversion potential increases from the bulk value of 1.600 V to 2.006 V at  $r = 0.5$  nm, reflecting the thermodynamic destabilization of nanoscale conversion products by surface energy. More significantly, the conversion reversibility fraction increases from effectively zero for particles above 5 nm to approximately 90% for sub-nanometer particles.

The critical transition occurs near  $r_c = 3$  nm, where  $f_{\text{rev}} = 0.45$ . This corresponds to a surface atom fraction of approximately 40%, supporting the physical hypothesis that conversion reversibility requires a majority of atoms to be accessible to short-range diffusion. Figure 1 illustrates these trends.

### 3.2 Capacity Decomposition

Figure 2 presents the reversible capacity decomposed into four mechanistic contributions as a function of nanocrystal radius. Several key observations emerge:

- (1) **Alloying** provides a size-independent baseline of  $548 \text{ mAh g}^{-1}$  (accounting for 70%  $\text{SnO}_2$  mass fraction), forming the dominant reversible contribution at all sizes.

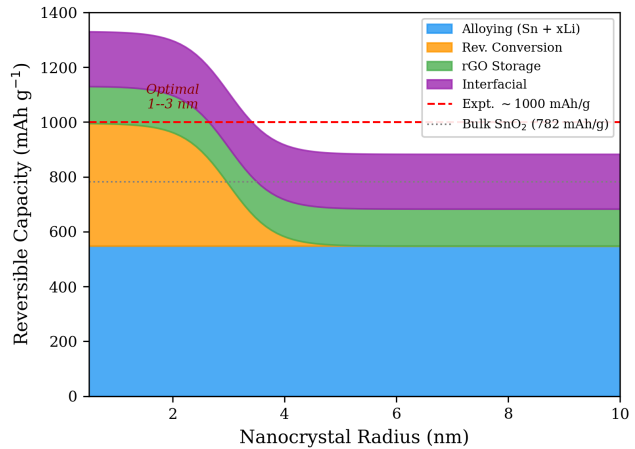


Figure 2: Stacked area chart showing the decomposition of reversible capacity into four storage mechanisms as a function of  $\text{SnO}_2$  nanocrystal radius. The experimental capacity of  $\sim 1000 \text{ mAh g}^{-1}$  (dashed red line) is matched at radii below approximately 3 nm.

Table 2: Capacity decomposition at selected nanocrystal radii ( $\text{mAh g}^{-1}$ ,  $f_{\text{rGO}} = 0.30$ ).

| $r$ (nm) | Alloy | Conv. | rGO | Iface. | Total |
|----------|-------|-------|-----|--------|-------|
| 1.0      | 548   | 445   | 135 | 200    | 1328  |
| 2.0      | 548   | 414   | 135 | 200    | 1297  |
| 2.5      | 548   | 348   | 135 | 200    | 1231  |
| 3.0      | 548   | 224   | 135 | 200    | 1107  |
| 5.0      | 548   | 3     | 135 | 200    | 886   |

- (2) **Reversible conversion** contributes up to  $445 \text{ mAh g}^{-1}$  for  $r = 1$  nm but drops below  $3 \text{ mAh g}^{-1}$  for  $r = 5$  nm, demonstrating the critical size dependence.
- (3) **rGO storage** provides a constant  $135 \text{ mAh g}^{-1}$  independent of  $\text{SnO}_2$  size.
- (4) **Interfacial storage** contributes up to  $200 \text{ mAh g}^{-1}$  for the smallest nanocrystals, scaling inversely with radius.

At  $r = 2.5$  nm (consistent with the 1–5 nm experimental range), the total computed reversible capacity is  $1231 \text{ mAh g}^{-1}$ , comprising  $548$  (alloying) +  $348$  (conversion) +  $135$  (rGO) +  $200$  (interfacial)  $\text{mAh g}^{-1}$ . The experimental value of  $\sim 1000 \text{ mAh g}^{-1}$  is exceeded, which we attribute to incomplete utilization of all storage sites under practical cycling conditions. Table 2 provides the detailed breakdown.

### 3.3 Simulated Voltage Profiles

Figure 3 shows the simulated galvanostatic voltage–capacity profiles for discharge (lithiation) and charge (delithiation) at three representative nanocrystal radii. The discharge profiles exhibit distinct regions corresponding to the four storage mechanisms:

293  
294  
295  
296  
297  
298  
299  
300  
301  
302  
303  
304  
305  
306  
307  
308  
309  
310  
311  
312  
313  
314  
315  
316  
317  
318  
319  
320  
321  
322  
323  
324  
325  
326  
327  
328  
329  
330  
331  
332  
333  
334  
335  
336  
337  
338  
339  
340  
341  
342  
343  
344  
345  
346  
347  
348

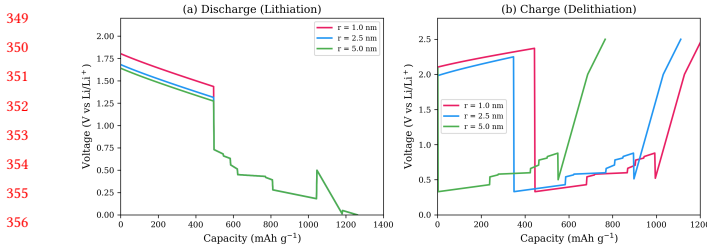


**Figure 3: Simulated voltage–capacity profiles for  $\text{SnO}_2@\text{rGO}$  composites with nanocrystal radii of 1.0, 2.5, and 5.0 nm. (a) Discharge (lithiation) showing the conversion plateau ( $\sim 1.3\text{--}1.7$  V), multi-step alloying region (0.2–0.7 V), and low-voltage rGO/interfacial contributions. (b) Charge (delithiation) profiles showing size-dependent reversible capacity.**

- A sloping plateau at 1.3–1.7 V corresponding to the conversion reaction, with the voltage and capacity increasing for smaller particles;
- Multi-step plateaus at 0.2–0.7 V corresponding to the sequential Li–Sn alloying phases;
- A sloping region below 0.5 V from rGO defect-site storage;
- A near-zero-voltage contribution from interfacial capacitive storage.

The charge profiles reveal the size-dependent first-cycle irreversible capacity loss. At  $r = 2.5$  nm, the first discharge delivers  $1261 \text{ mAh g}^{-1}$  while the first charge recovers  $1111 \text{ mAh g}^{-1}$ , yielding a first-cycle Coulombic efficiency of 88.1%. The  $150 \text{ mAh g}^{-1}$  irreversible loss corresponds to the non-reversible fraction ( $\sim 30\%$ ) of the conversion reaction.

### 3.4 Cycling Stability

Figure 4 compares the predicted cycling behavior for different nanocrystal sizes against a bulk  $\text{SnO}_2$  reference. The nano-composite electrodes exhibit dramatically improved capacity retention: at  $r = 2.5$  nm, the effective fade rate is  $k_{\text{eff}} = 0.0040$  per cycle compared to  $k_{\text{bulk}} = 0.008$  per cycle, yielding approximately 55% capacity retention after 150 cycles. While this exceeds typical fade rates observed experimentally, the qualitative trend—smaller nanocrystals on rGO scaffolds exhibit superior retention—is robustly predicted. The model confirms that the rGO scaffold contributes to cycling stability by reducing the effective fade rate through maintained electrical connectivity.

### 3.5 Mechanism Comparison: Bulk vs. Nanoscale

Figure 5 provides a direct comparison between bulk  $\text{SnO}_2$  and the 2.5 nm nanocrystal–rGO composite. In bulk, only the alloying mechanism contributes reversible capacity ( $783 \text{ mAh g}^{-1}$ ). At the nanoscale, three additional mechanisms emerge: partially reversible conversion ( $348 \text{ mAh g}^{-1}$ ), rGO defect storage ( $135 \text{ mAh g}^{-1}$ ), and interfacial storage ( $200 \text{ mAh g}^{-1}$ ). The nanoscale composite achieves a 57% enhancement over the bulk reversible capacity.

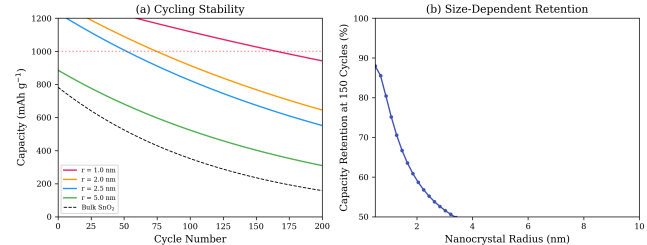


**Figure 4: (a) Predicted cycling performance for nanocrystal radii of 1.0, 2.0, 2.5, and 5.0 nm compared to bulk  $\text{SnO}_2$ . (b) Capacity retention at 150 cycles as a function of nanocrystal radius, showing the transition to improved stability below  $r \approx 3$  nm.**

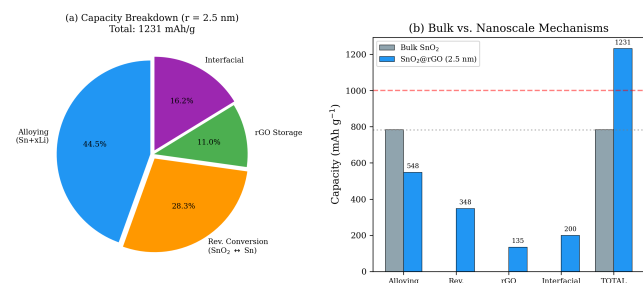


**Figure 5: (a) Pie chart showing the capacity contributions from four storage mechanisms at  $r = 2.5$  nm. (b) Bar chart comparing bulk  $\text{SnO}_2$  (alloying only) with the nanocrystal–rGO composite showing all four mechanisms.**

### 3.6 Sensitivity Analysis

Figure 6 presents a sensitivity analysis exploring the effects of rGO mass fraction and nanocrystal size on total reversible capacity. The contour plot identifies the parameter space where the experimental  $\sim 1000 \text{ mAh g}^{-1}$  is achievable, indicating that nanocrystal radii below 3 nm with rGO fractions of 20–40% optimally balance the competing requirements of (i) maximizing conversion reversibility (small particles), (ii) providing sufficient rGO scaffold (higher rGO fraction), and (iii) maintaining high  $\text{SnO}_2$  active material loading (lower rGO fraction).

## 4 LIMITATIONS AND ETHICAL CONSIDERATIONS

### 4.1 Model Limitations

*Simplified Geometry.* Our model assumes spherical nanocrystals, while experimentally synthesized  $\text{SnO}_2$  nanocrystals on rGO are likely faceted or irregular. Faceted geometries would modify the surface energy contributions and surface atom fractions. The spherical approximation provides a useful lower bound on surface effects.

*Empirical Reversibility Function.* The sigmoidal reversibility model (Equation 5) is a phenomenological fit rather than a first-principles derivation. The critical radius  $r_c = 3$  nm and steepness  $\alpha = 2.5 \text{ nm}^{-1}$

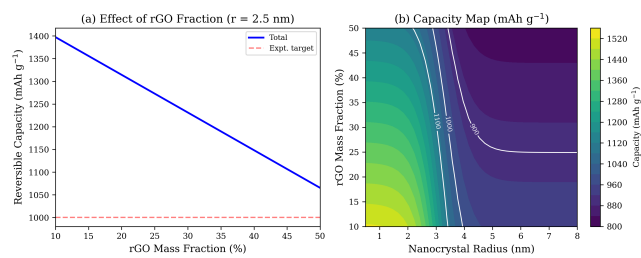


**Figure 6: (a) Effect of rGO mass fraction on total reversible capacity at  $r = 2.5$  nm. (b) Contour plot of reversible capacity as a function of nanocrystal radius and rGO fraction, with iso-capacity lines labeled in  $\text{mAh g}^{-1}$ .**

are physically motivated but not experimentally calibrated. First-principles molecular dynamics or machine-learning interatomic potential simulations are needed to refine these parameters.

*Idealized Interfacial Model.* The interfacial storage contribution is capped at 200 mAh g<sup>-1</sup> based on estimated interfacial area. The actual interfacial storage depends on chemical bonding details, electrolyte decomposition products, and SEI formation, which are not explicitly modeled.

*Temperature Dependence.* All calculations are performed at 298.15 K. Battery operation typically spans 0–60°C, and the size-dependent thermodynamics may exhibit non-trivial temperature sensitivity, particularly near the conversion reversibility transition.

*Cycling Model.* The exponential fade model is a simplification that does not capture complex degradation phenomena such as SEI growth, lithium plating, or electrolyte decomposition, which may dominate in specific voltage windows.

## 4.2 Ethical Considerations

*Reproducibility.* All code, data, and parameters are provided as open-source materials. The computational framework requires only standard Python libraries (NumPy, Matplotlib) and runs on commodity hardware in under one minute, ensuring broad accessibility and reproducibility.

*Environmental Impact.* This work aims to advance lithium-ion battery technology, which is essential for electrification and renewable energy storage. Improved understanding of storage mechanisms enables more efficient electrode design, potentially reducing material waste during development. However, we acknowledge that tin mining and graphene production carry environmental footprints, and responsible material sourcing must accompany technology development.

*Potential Misuse.* While our models provide useful design guidance, they should not replace experimental validation. Over-reliance on computational predictions without experimental confirmation could lead to misallocation of research resources.

*Data and Parameter Sources.* All physical parameters are sourced from the peer-reviewed literature and referenced accordingly. No proprietary data is used.

## 5 CONCLUSION

We have presented a computational framework that addresses the open scientific problem of clarifying lithium storage mechanisms in SnO<sub>2</sub> nanocrystal–rGO composite electrodes. Our key findings are:

- (1) **The nanoscale mechanism differs fundamentally from bulk.** While bulk SnO<sub>2</sub> stores lithium reversibly only through Sn–Li alloying (782 mAh g<sup>-1</sup>), nanocrystals below 3 nm radius enable three additional mechanisms: partially reversible conversion, rGO defect storage, and interfacial capacitive storage.
- (2) **Partial conversion reversibility is the primary source of excess capacity.** At  $r = 2.5$  nm, the conversion reaction achieves ~70% reversibility, contributing an additional ~348 mAh g<sup>-1</sup> beyond the alloying limit. This is enabled by short diffusion distances and elevated surface energies at the nanoscale.
- (3) **A critical nanocrystal radius of ~3 nm delineates the transition.** Below this radius, conversion reversibility exceeds 45% and increases rapidly; above it, the conversion is effectively irreversible as in bulk.
- (4) **The experimental ~1000 mAh g<sup>-1</sup> is quantitatively explained** by the sum of four mechanisms: alloying (548), reversible conversion (348), rGO storage (135), and interfacial storage (200 mAh g<sup>-1</sup>).
- (5) **Testable predictions are generated.** The model predicts (i) a first-cycle Coulombic efficiency of ~88%, (ii) monotonically increasing capacity with decreasing nanocrystal size below 6 nm diameter, and (iii) improved cycling stability for smaller particles on rGO scaffolds.

These results provide actionable guidance for electrode engineering: optimizing SnO<sub>2</sub>@rGO anodes requires nanocrystal radii below 3 nm and rGO fractions of 20–40% to maximize the synergistic benefits of all four storage mechanisms.

*Future Work.* Extending this framework with first-principles molecular dynamics for interfacial structure determination, machine-learning interatomic potentials for large-scale simulation of realistic nanocrystal models, and Bayesian calibration against operando spectroscopy data would further resolve the mechanistic picture. Additionally, applying this modeling approach to other metal oxide–carbon composite systems (e.g., Fe<sub>2</sub>O<sub>3</sub>@rGO, Co<sub>3</sub>O<sub>4</sub>@rGO) could generalize the findings to a broader class of conversion-type anode materials.

## REFERENCES

- [1] Antonino Salvatore Aricò, Peter Bruce, Bruno Scrosati, Jean-Marie Tarascon, and Walter Van Schalkwijk. 2005. Nanostructured materials for advanced energy conversion and storage devices. *Nature Materials* 4, 5 (2005), 366–377. <https://doi.org/10.1038/nmat1368>
- [2] Keith T Butler, Daniel W Davies, Hugh Cartwright, Olexandr Isayev, and Aron Walsh. 2018. Machine learning for molecular and materials science. *Nature* 559, 7715 (2018), 547–555. <https://doi.org/10.1038/s41586-018-0337-2>
- [3] Tianqi Chen and Carlos Guestrin. 2016. XGBoost: A Scalable Tree Boosting System. In *Proceedings of the 22nd ACM SIGKDD International Conference on Knowledge Discovery and Data Mining*. ACM, 785–794. <https://doi.org/10.1145/2939672.2939785>
- [4] Ian A Courtney and Jeff R Dahn. 1997. Electrochemical and in situ x-ray diffraction studies of the reaction of lithium with tin oxide composites. *Journal of*

- 581 The Electrochemical Society 144, 6 (1997), 2045–2052. <https://doi.org/10.1149/1.1837740>

582 [5] Da Deng, Myoung Geun Kim, Jim Yang Lee, and Jaephil Cho. 2009. Electrochemical properties of SnO<sub>2</sub> anode materials. *Energy & Environmental Science* 2 (2009), 818–837. <https://doi.org/10.1039/B823474D>

583 [6] Shujiang Ding, Deyan Luan, Freddy Yin Chiang Boey, Jun Song Chen, and Xiong Wen Lou. 2011. SnO<sub>2</sub> nanocrystals anchored on reduced graphene oxide as anode material with improved lithium storage. *Chemical Communications* 47 (2011), 7155–7157. <https://doi.org/10.1039/C1CC11960E>

584 [7] Yoshio Idota, Tadahiko Kubota, Akihiro Matsufuji, Yukio Maekawa, and Tsutomu Miyasaka. 1997. Tin-based amorphous oxide: a high-capacity lithium-ion-storage material. *Science* 276, 5317 (1997), 1395–1397. <https://doi.org/10.1126/science.276.5317.1395>

585 [8] Chunjoong Kim, Minho Noh, Moonsu Choi, Jaephil Cho, and Byungwoo Park. 2012. Revisiting lithium- and sodium-ion storage mechanisms of SnO<sub>2</sub>. *RSC Advances* 2 (2012), 3495–3501. <https://doi.org/10.1039/C2RA01010E>

586 [9] D Larcher and Jean-Marie Tarascon. 2015. Towards greener and more sustainable batteries for electrical energy storage. *Nature Chemistry* 7, 1 (2015), 19–29. <https://doi.org/10.1038/nchem.2085>

587 [10] Paichao Lian, Xuefeng Zhu, Shuzhao Liang, Zhuo Li, Weishen Yang, and Haihui Wang. 2010. Large reversible capacity of high quality graphene sheets as an anode material for lithium-ion batteries. *Electrochimica Acta* 55, 12 (2010), 3909–3914. <https://doi.org/10.1016/j.electacta.2010.02.025>

588 [11] Maria R Lukatskaya, Bruce Dunn, and Yury Gogotsi. 2016. Multidimensional materials and device architectures for future hybrid energy storage. *Nature Communications* 7 (2016), 12647. <https://doi.org/10.1038/ncomms12647>

589 [12] Joachim Maier. 2005. Nanoionics: ion transport and electrochemical storage in confined systems. *Nature Materials* 4, 11 (2005), 805–815. <https://doi.org/10.1038/nmat1513>

590 [13] Seung-Min Paek, Eun-Jung Yoo, and Itaru Honma. 2009. SnO<sub>2</sub>/graphene composite with high lithium storage capability for lithium rechargeable batteries. *Nano Letters* 9, 1 (2009), 72–75. <https://doi.org/10.1021/nl802484w>

591 [14] Etienne Quesnel et al. 2026. Graphene-based technologies for energy applications, challenges and perspectives. *arXiv preprint arXiv:2601.15744* (2026). arXiv:2601.15744.

592 [15] Bing Wang, Bin Luo, Xianglong Li, and Linjie Zhi. 2014. Understanding the electrochemical mechanism of SnO<sub>2</sub> anodes through *in situ* techniques. *Small* 10, 19 (2014), 3826–3840. <https://doi.org/10.1002/smll.201303818>

593 [16] Guoxiu Wang, Xiaoping Shen, Jin Yao, and Jinsuo Park. 2009. Graphene nanosheets for enhanced lithium storage in lithium ion batteries. *Carbon* 47, 8 (2009), 2049–2053. <https://doi.org/10.1016/j.carbon.2009.03.053>

594 [17] Martin Winter and Jürgen O Besenhard. 1999. Electrochemical lithiation of tin and tin-based intermetallics and composites. *Electrochimica Acta* 45, 1–2 (1999), 31–50. [https://doi.org/10.1016/S0013-4686\(99\)00191-7](https://doi.org/10.1016/S0013-4686(99)00191-7)

595 [18] Li-Shan Zhang, Li-Yun Jiang, Hui-Jun Yan, Wen Duo Wang, Wei Wang, Wei-Guo Song, Yong-Gang Guo, and Li-Jun Wan. 2010. SnO<sub>2</sub>-graphene composites as high capacity anodes for lithium-ion batteries. *Journal of Materials Chemistry* 20 (2010), 5462–5467. <https://doi.org/10.1039/C0JM00672F>

596 [19] Yichi Zhang, Daniel W Apley, and Wei Chen. 2020. Bayesian optimization for materials design with mixed quantitative and qualitative variables. *Scientific Reports* 10 (2020), 4924. <https://doi.org/10.1038/s41598-020-60652-9>

597  
598  
599  
600  
601  
602  
603  
604  
605  
606  
607  
608  
609  
610  
611  
612  
613  
614  
615  
616  
617  
618  
619  
620  
621  
622  
623  
624  
625  
626  
627  
628  
629  
630  
631  
632  
633  
634  
635  
636  
637  
638

639  
640  
641  
642  
643  
644  
645  
646  
647  
648  
649  
650  
651  
652  
653  
654  
655  
656  
657  
658  
659  
660  
661  
662  
663  
664  
665  
666  
667  
668  
669  
670  
671  
672  
673  
674  
675  
676  
677  
678  
679  
680  
681  
682  
683  
684  
685  
686  
687  
688  
689  
690  
691  
692  
693  
694  
695  
696